Journal of Colloid and Interface Science 664 (2024) 561–572

Contents lists available at ScienceDirect

Journal of Colloid And Interface Science

journal homepage: www.elsevier.com/locate/jcis

Interfacial processes underlying the temperature-dependence of friction and wear of calcite single crystals

Binxin Fu [a], Rosa M. Espinosa-Marzal [a,b,*]

[a] Department of Civil and Environmental Engineering, University of Illinois at Urbana-Champaign, 205 N. Matthews Avenue, Urbana, IL 61801, United States
[b] Department of Materials Science and Engineering, University of Illinois at Urbana-Champaign, 1304 W. Green St., IL 618101, United States

GRAPHICAL ABSTRACT

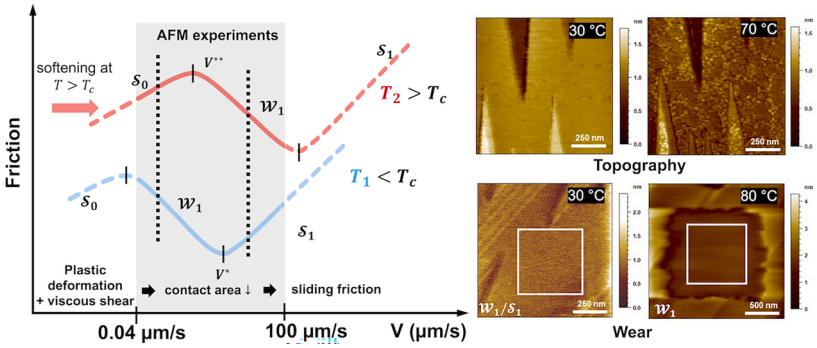

ARTICLE INFO

Keywords:
Calcite
Friction
Wear
Temperature
Atomic force microscopy
Surface reconstruction

ABSTRACT

Hypothesis: This study posits that thermal effects play a substantial role in influencing interfacial processes on calcite, and consequently impacting its mechanochemical properties.
Experiments: This work interrogates the temperature-dependence of friction and wear at nanoscale contacts with calcite single crystals at low air humidity (≤ 3–10 % RH) by AFM.
Findings: Three logarithmic regimes for the velocity-dependence of friction are identified. BelowT_c ~ 70 °C, where friction increases with T, there is a transition from velocity-weakening ($\mathscr{W}_1$) to velocity-strengthening friction ($\mathscr{S}_1$). AboveT_c ~ 70 °C, where friction decreases with T, a second velocity-strengthening friction regime ($\mathscr{S}_0$) precedes velocity-weakening friction ($\mathscr{W}_1$). The low humidity is sufficient to induce atomic scale changes of the calcite cleavage plane due to dissolution-reprecipitation, and more so at higher temperature and 10 % RH. Meanwhile, the surface softens above T_c –likely owing to lattice dilation, hydration and amorphization. These interfacial changes influence the wear mechanism, which transitions from pit formation to plowing with increase in temperature. Furthermore, the softening of the surface justifies the appearance of the second velocity-strengthening friction regime ($\mathscr{S}_0$).

Abbreviations: AFM, atomic force microscopy; DMT, Derjaguin, Muller, and Toporov; HT-XRD, high temperature x-ray diffraction; MD, molecular dynamic; PT, Prandtl-Tomlinson; T, temperature; RH, relative humidity; RT, room temperature; UHV, ultra-high vacuum.

* Corresponding author.
E-mail address: rosae@illinois.edu (R.M. Espinosa-Marzal).

https://doi.org/10.1016/j.jcis.2024.03.035
Received 21 January 2024; Received in revised form 4 March 2024; Accepted 5 March 2024
Available online 6 March 2024
0021-9797/© 2024 The Authors. Published by Elsevier Inc. This is an open access article under the CC BY-NC-ND license (http://creativecommons.org/licenses/by-nc-nd/4.0/).

These findings advance our understanding of the influence of temperature on the interfacial and mechano-chemical processes involving calcite, with implications in natural processes and industrial manufacturing.

1. Introduction

Calcite, one of the most abundant minerals in nature, is involved in several environmental and geochemical processes [1–4]. Calcite powder and granulate find widespread use in construction and steelmaking industry, as well as serving as filler or pigment in the manufacturing of paper, pulp, paints, plastics, rubbers, chemicals, and pharmaceuticals [5]. The calcite/water interface has received great attention among the past years, revealing unique characteristics of structure, ion adsorption capacity, and reactivity in different environments [6–17].

Calcite undergoes significant surface reconstruction upon exposure to air already at low relative humidity (RH) [8,18]. Synchrotron X-ray reflectivity[19] has revealed that water molecules adsorb on the $(10\bar{1}4)$ plane of calcite upon cleavage in air to satisfy dangling bonds and remain there even after ultra-high vacuum (UHV) treatment [20]. Molecular dynamic (MD) simulations indicate that, independently of the RH, the water distribution on the calcite surface is nonuniform and even in the case of a perfect (defect-free) surface, dry patches constantly appear and disappear [21]. While the non-uniform distribution of water appears to be consistent with the non-uniform formation of hillocks and trenches, several experimental studies report, instead, the formation of a complete water monolayer already at low humidity ~ 10–20 % RH, and even lower humidity given sufficient time [8]; for more details, see review [17] and references herein. The roughness and cleanness of the surface also plays a role in the characteristics of the adsorbed water layers [17]. The reconstruction of the calcite surface presumably arises from the presence of adsorbed water on the calcite surface. Based on the ion diffusion model, the surface-adsorbed water molecules lead to dissolution at high-energy sites (vacancy defects, edges and steps) and thereby to pit formation, while ion diffusion evens concentration gradients within the water layer and carries these ions somewhere else. When the liquid film is supersaturated, hillocks start growing on favorable sites at the terraces [18,22]. The height of the hillocks varies between one to ten calcite monolayers, each ~ 3 Å.

The friction between calcite particles is of significance in manufacturing processes involving handling, grinding, milling, mixing, or blending. There is a direct link between particle–particle interactions and macroscopic properties like flowability and cohesion [23]. Understanding and controlling friction and wear between calcite particles as well as the tribochemically induced reactions -"tribo" is the Greek concept for rubbing or wearing away- in function of hydrothermal conditions is crucial in optimizing many manufacturing processes since it can influence the efficiency of the equipment, the quality of the final product, and the overall production costs[24]. In addition to this, geophysical studies propose a link between the frictional characteristics of minerals and the mechanisms underlying fault slip, and earthquake nucleation [25–29]. This is because, despite the enormous discrepancy in length scales, the fault strength relies on the friction force at single asperity contacts.

Atomic Force Microscopy (AFM) in contact mode is widely used to investigate the tribochemical behavior of nanoscale single asperity contacts [30–32]. While AFM experiments are highly simplified compared to the complexity in nature and industrial processes, they allow isolating phenomena to investigate underlying physical and chemical mechanisms [25–29]. Prior studies of the frictional and adhesive behavior of calcite's atomically smooth $(10\bar{1}4)$ cleavage plane conducted by AFM are summarized in Table S1. Park's and Dickinson's pioneering AFM scratching tests on a single calcite crystal in saturated $CaCO_3$ solution demonstrated that contact pressure enhances wear rate across atomic steps [33–35]. Diao & Espinosa-Marzal investigated the influence of the aqueous (liquid) environment on single-asperity calcite friction and revealed that the pressure-induced dissolution of calcite can cause a significant reduction of friction at sufficiently high stresses and slow sliding velocities, a phenomenon called "pressure-solution facilitated slip" [27]. Subsequent studies demonstrated the specific influence of the solution composition on pressure solution and pressure-solution facilitated slip [36,37]. The wear resistance and nanomechanical properties of bare calcite and stearic acid-modified calcite surfaces in dry and humid (75 % RH) air have been also studied by AFM at room temperature (RT) [38]. The sliding motion is characterized by irregular stick–slip, especially when water is adsorbed on the calcite surface, and it leads to wear at sufficiently high applied loads. When exposed to humid air, the friction force is similar to that in dry air, but the wear depth is reduced. The latter was attributed to the influence of water on the distribution of wear particles. More recently, the influence of nanoscale roughness on calcite friction was investigated both in dry nitrogen and aqueous environment by AFM [29]. The combined measurements revealed that atomic attrition is responsible for the wear of the dry calcite surface at RT; because longer contact times (slower velocity) promote atomic attrition, this abrasive phenomenon justifies the decrease of friction with velocity. Increasing surface roughness of the dry calcite, however, was shown to reverse this trend to a logarithmic increase of friction with velocity. In contrast, the frictional response in aqueous solution is dominated by the pressure solution of calcite, which leads to a linear increase of friction with velocity [29].

For both natural and industrial processes, understanding the influence of humidity and thermal conditions on surface structure, frictional and wear properties of calcite is crucial. In the present study, we advance the current knowledge by investigating the influence of temperature on the frictional and wear characteristics of the $(10\bar{1}4)$ cleavage plane of Iceland Spar calcite single crystals using high-resolution AFM. Here, the relative humidity was set at 10 % RH and $\leq$ 3 % RH. These experimental studies let us propose various mechanisms underlying the complex temperature-dependent tribochemical behavior of calcite in a low humidity environment.

2. Materials and methods

A Cypher ES Environmental AFM (Asylum Research, Oxford Instrument) was used to measure friction force and image calcite single crystals. AFM experiments were performed with the same AFM cantilever type (CSC38/no Al, Mikromasch) with normal spring constants ranging between 0.1 and 0.3 N m^{-1} and a sharp Si tip. The cantilevers were thermally annealed at 1050 °C for 2 h to increase the tip radius and thereby to avoid their damage during the experiments. The radius of the tips used in the reported experiments range from 35 to 61 nm, as determined by inverse AFM imaging of a test grating (TGTZ-400, TED PELLA, INC); Fig. S1. The Derjaguin, Muller, and Toporov (DMT) contact mechanics model was applied to estimate contact pressures (Table S2) at single asperity contacts between the tip and the calcite surface. Tips were rinsed with pure ethanol for 30 min and UV cleaned for 50 min prior to use. The calcite surfaces were prepared by cleaving Iceland Spar Calcite crystals along the $(10\bar{1}4)$ plane right before use.

The AFM chamber was purged with dry nitrogen to decrease the humidity. Two different set-ups were used (Fig. S2a). First, a N_2 gas tube was connected to the side of the Cypher AFM chamber at ~ 2 CFH, which led to ~ 10 % RH as determined by a hygrometer. Second, the gas tube was extended to the environmental cell to achieve a lower RH, which maintained the humidity to $\leq$ 3 % RH in the cell (labeled as 3 % RH). At the low humidity of these experiments a capillary meniscus did

not form between the calcite surface and the tip, and hence, the action of capillary forces was avoided. The temperature in the AFM chamber was controlled from RT (24 ± 1 °C) to 120 °C, with temperature variations smaller than 0.1 K during experiments. The thermal calibration of the tip sensitivity and normal spring constant was performed at each temperature [39].

2.1. Friction measurements

Friction force measurements were performed by sliding the AFM tip along the ($10\bar{1}4$) plane of calcite. As the AFM tip slides on the surface, it experiences a lateral force due to friction force between tip and calcite, which leads to a lateral deflection of the cantilever. The lateral spring constant was obtained by a noncontact thermal noise-based calibration method [40], and the lateral force was determined by multiplying lateral spring constant and lateral deflection during both trace and retrace. A single crystal was used in each experiment (4 experiments at 10 % RH, and two at 3 % RH) and exposed sequentially to a higher temperature. The location of the measurement was changed every time the temperature was changed and at least 1 h equilibration time was given before the measurement started at each temperature.

For the velocity-dependent friction measurements, the sliding velocity was varied from 0.04 to 100 μm s^{-1}. To examine this wide range of velocities, the sliding length was increased from 200 nm to 10 μm. Friction measurements were carried out at loads of 10, 50, and 100 nN, and at temperatures between RT and 120 °C. The friction force is calculated as the half of the difference between the trace and retrace lateral force for each friction loop. Sixteen trace/retrace scans (loops) were measured at each load and velocity (Fig. S2b); the plots show the average friction force, and the error bars represent the standard deviation, which is often smaller than the marker size, and hence, not always visible. In load-dependent friction measurements, the load was varied from 10 to 90 nN and the scan distance was kept at 100 nm. The measurements were performed at 0.2 and 2 μm s^{-1} and at three temperatures per sliding velocity (30, 50 and 80 °C). The wear of the tip was controlled throughout the duration of the experiments by determining the tip radius by inverse image of an AFM grating and measuring the pull-off force between the tip and a silicon wafer, since any change of the tip geometry would be reflected in a change of the pull off force. While we cannot completely rule out that the oxide layer covering the surface of the tip was removed when the tip made contact with the calcite surface [41], silicon is much harder than calcite, and hence, the wear of the calcite surface should be predominant. Indeed, no significant changes in tip size were noticed during the friction force measurements on each single crystal.

2.2. Calcite surface imaging

AFM images were taken in tapping mode at a scan rate of 1 Hz with a gold-coated tapping mode tip (Tap300GD-G, normal spring constant = 40 N m^{-1}, resonance frequency = 300 kHz; Budget Sensors). Height, amplitude and phase images were captured at temperatures between RT and 90 °C. The equilibrium time at each temperature ranged between 1 and 1.5 h.

2.3. Wear measurements

Wear measurements were carried out by contact mode imaging both at 10 % and 3 % RH. The measurements were performed at 0.2, 1, and 10 μm s^{-1} and at three temperatures (30, 50, and 90 °C) per sliding velocity. The topography of the surface prior to the wear measurements was captured in a relatively smooth region (1 μm × 1 μm) to eliminate the effect of defects, and a small load of 5 nN was applied to avoid wear of the surface. Ten contact mode images (0.5 μm x 0.5 μm) at normal load of 100 nN were taken in the middle of the smooth area. After the high-load imaging, the same larger surface 1 μm × 1 μm was imaged again at low load. The calcite crystal was equilibrated at the selected temperatures for 30 min preceding the wear experiment.

2.4. Adhesion measurements

Force maps (10 × 10) were carried out on a 150 nm × 150 nm area on freshly cleaved calcite crysals with a sharp Si tip. The approach tip velocity was set at 0.15 μm s^{-1} and the z-length at 0.5 μm for each force curve in the map. The force maps were performed at RT, 40 °C, 50 °C, 60 °C, and 80 °C with a maximum normal load of 10 nN. An equilibrium time of at least 1 h was ensured every time the temperature was varied.

2.5. Crystallinity measurements

The crystallinity of the cleaved calcite pieces was determined by RT XRD (Siemens-Bruker, D5000, Cu-K alpha source, 0.15418 nm, USA). The samples were pre-heated in an oven at 150 °C for 2 h right before the measurement. XRD diffractograms were collected between 2θ angles of 10 and 70° at a scan speed of 5° min^{-1} at RT. High temperature (HT) XRD was also used to characterize the crystallinity of calcite. Here, the temperature varied from room temperature to 150 °C in Argon. The heating rate was 10 °C min^{-1} and scanning parameters were the same as in RT XRD. The peak search, background removal and crystallinity computing of the XRD curves were performed with the software Bruker EVA.

3. Results and discussion

Isothermal friction-force measurements were carried out with oxidized silicon tips sliding on the freshly cleaved ($10\bar{1}4$) plane of single calcite crystals in reciprocating motion at velocities from 0.04 to 100 μm s^{-1}. The applied load was varied between 10 and 100 nN, corresponding to normal pressures in the range 207 MPa-1.4 GPa (Table S2), and temperatures ranging between RT and 120 °C. Experimental details can be found in the Methods Section and the setup in Fig. S2. Considering the high reactivity of calcite in humid environments [8,18,21,42], two different set-ups were used to control the relative humidity at i) ~ 10 % RH and ii) ≤ 3 % RH (labeled as dry); note that both low-humidity conditions lead to adsorption of water on the calcite surface [19].

3.1. The effect of temperature on calcite friction

Fig. 1 shows the friction force (F) between the tip and calcite as a function of sliding velocity (V), at three normal loads (L) and various temperatures (T) at 10 % RH. At 25 °C (Fig. 1a), the friction force exhibits a logarithmic decrease with velocity, i.e., $F/L\ \beta_1 \bullet \ln(V)$, with $\beta_1 < 0$ –labelled as velocity-weakening friction ($\mathscr{W}_1$) regime. At $V > 1$ μm s^{-1}, friction increases logarithmically with velocity, i.e., $F/L\ \alpha_1 \bullet \ln(V)$ with $\alpha_1 > 0$ –labeled as velocity-strengthening friction ($\mathscr{S}_1$) regime. V^* is the velocity at the transition between $\mathscr{W}_1$ and $\mathscr{S}_1$, whereas β_1 and α_1 are the rate parameters that characterize the velocity dependence of the friction force, respectively. The results are in qualitative agreement with our previous studies at 0 % RH and RT [29]. The fits are shown in Fig. S3, and Tables S3-4 display the average fitting rate parameters from multiple experiments.

Both velocity-weakening and strengthening friction ($\mathscr{W}_1$ and $\mathscr{S}_1$) regimes persist at 40 and 50 °C. The $\mathscr{S}_1$ regime extends over a wider range of velocities with increase in temperature and load (normal stress). As the temperature increases further to 60 °C (Fig. 1d), the $\mathscr{W}_1$ regime is not resolved anymore, presumably because it shifts to slower sliding velocities that cannot be attained with our AFM (i.e., $V^* < 0.04$ μm s^{-1}).

Fig. 1e–f displays an abrupt change of the frictional characteristics when the temperature increases to 80 °C and 90 °C. Here, friction

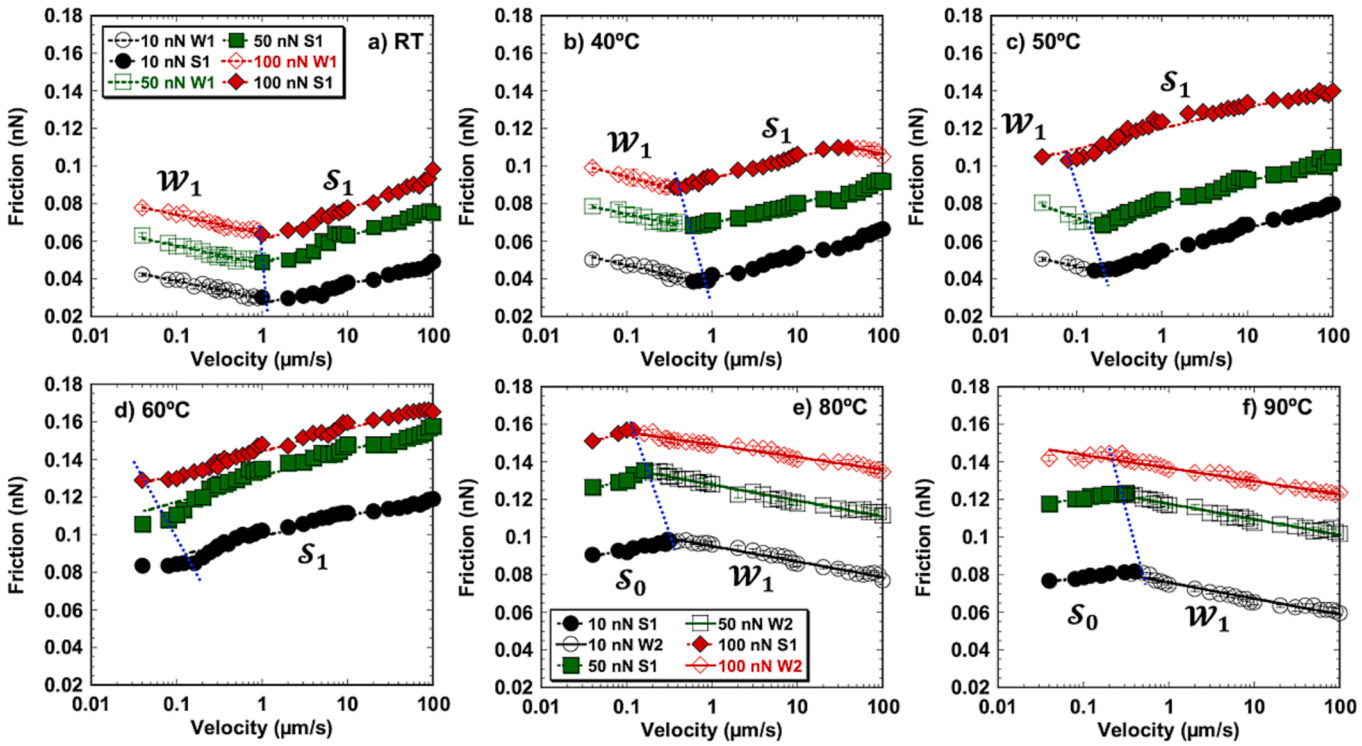

Fig. 1. Friction force between a thermally oxidized Si tip and calcite as a function of sliding velocity and normal load at 10 % RH. Selected temperatures are **a)** RT, **b)** 40 °C, **c)** 50 °C, **d)** 60 °C, **e)** 80 °C, and **f)** 90 °C. The system is equilibrated for at least 1 h at each temperature. The marker legend is as follows: black circles for 10 nN, green squares for 50 nN, and red diamonds for 100 nN. The error bars give the standard variation in friction over at least 16 friction loops but they are often smaller than the marker size and therefore not always visible. The lines illustrate the logarithmic change of friction during first velocity-weakening $\mathscr{W}_1$ regime (dash line), velocity-strengthening $\mathscr{S}_1$ regime (dot-dash line) at $T < T_c$ and second velocity-strengthening S_0 regime (solid line) followed by the weakening regime $\mathscr{W}_1$. Two other experiments on different calcite single crystals are included in Figs. S4-5.

increases over a very narrow range of velocities. Above a transition velocity (V^{**}), friction decreases with the logarithm of velocity, i.e., $F/L\ \beta_1 \ln(V)$, $\beta_1 < 0$ at $V > V^{**}$. Thus, this abrupt change reveals a new velocity-strengthening regime, $F/L\ \alpha_0 \bullet \ln(V)$ with $\alpha_0 > 0$ –labeled as $\mathscr{S}_0$ regime– that precedes the $\mathscr{W}_1$ regime. These results are confirmed in experiments with other calcite single crystals and temperatures up to 120 °C; see e.g. Figs. S4-5. Fig. 2 displays the change of friction with temperature from four experiments with different calcite crystals and tips at 10 % RH. Each plot displays the results at one velocity (0.04, 1 and 10 μm s^{-1}, respectively) and a normal load of 50 nN. Despite the friction variation across experiments, the general trend is that friction increases with temperature and then it decreases. In some experiments, only a plateau regime above T_c was observed, likely because the temperature was not high enough for the onset of the decrease in friction. The maximum in friction is observed at a critical temperature T_c between 60 and 80 °C, with a subtle increase of T_c with increasing load and decreasing velocity. The plots of friction vs. temperature under applied loads of 10 nN and 100 nN are qualitatively similar (Fig. S6). With increase (decrease) in load, the data points shift upwards (downwards). In the following, T_c is taken at 70 °C for simplification.

3.2. Influence of the humidity on calcite friction

A set of friction measurements was carried out at ≤ 3 % RH (Fig. S7). In brief, there is (i) velocity-weakening friction ($\mathscr{W}_1$) followed by strengthening ($\mathscr{S}_1$) at temperatures ≤ 60 °C, (ii) a peak in friction at ~ 60 °C (T_c), and (iii) a $\mathscr{S}_0$ regime substituted by a close to velocity-neutral friction regime, followed by velocity-weakening friction ($\mathscr{W}_1$)

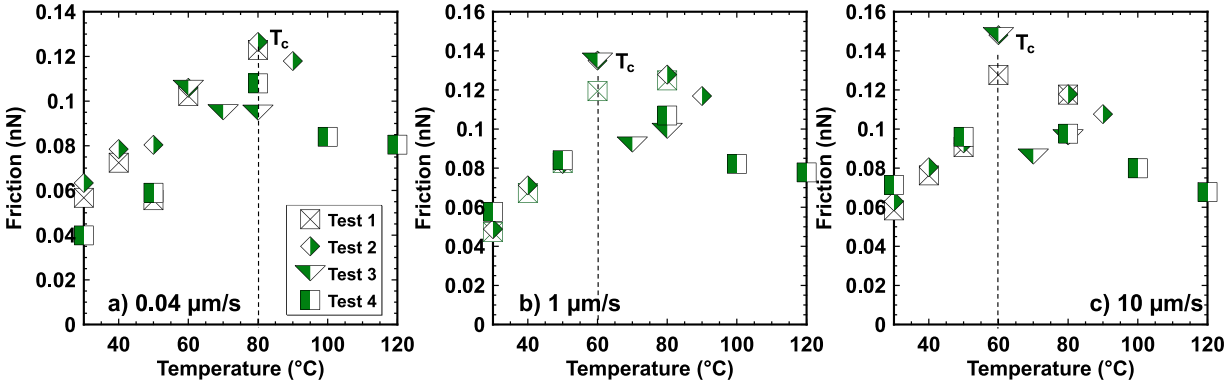

Fig. 2. Friction force as a function of temperature. The data are shown at sliding velocities of **a)** 0.04, **b)** 1, and **c)** 10 μm s^{-1} and at an applied load of 50 nN. The relative humidity was maintained constant at 10 % RH. Data from experiments with different calcite crystals and tips are indicated as tests 1–4.

above 60 °C. While the maximum friction happens at a similar temperature, the peak is much narrower than at 10 % RH (*cf.* Fig. S7f and Fig. 2).

The transition velocities V^* and V^{**} at both humidity conditions are displayed in Fig. 3**a**. At 10 % RH and 25 °C, the velocity at the crossover between $\mathscr{W}_1$ and $\mathscr{S}_1$ friction regimes (full box, V^*) is broadly distributed between 0.6 and 1 μm s^{-1}. As the temperature increases to 40 °C and 50 °C, V^* drops to 0.3–0.6 μm s^{-1}, and 0.08–0.16 μm s^{-1}, respectively; at 60 °C, V^* is close to 0.04 μm s^{-1}, although it cannot be determined with high precision. The distribution of V^* at each temperature is related to the effect of load (contact stress); an increase in load leads to a decrease in V^*, that is, it shifts the $\mathscr{S}_1$ friction regime to smaller sliding velocities. Hence, the $\mathscr{S}_1$ regime ($V > V^*$) extends over a wider range of velocities with increase in temperature and stress. The results at RT are in qualitative agreement with our previous studies at 0 % RH [29]. The smaller tip radius used here leads to higher contact stress, and thereby, to smaller values of V^* (and rate parameters) compared to our previous work. The decrease of V^* with temperature coincides with our previous observation that V^* decreases with roughness at RT, thereby yielding a wider velocity-strengthening regime [29], and as demonstrated later, the roughness increases with temperature. Above T_c, the transition velocity between $\mathscr{S}_0$ and $\mathscr{W}_1$ (V^{**}, striped box) appears to increase with temperature, which implies that the $\mathscr{S}_0$ regime ($V < V^{**}$) extends over a wider range of velocities, as well. At ≤ 3 % RH, the transition velocity V^* (V^{**}) is a bit larger (smaller) than the average values at 10 % RH, which implies the $\mathscr{W}_1$ regime is promoted above and below T_c at lower RH; see circles and triangles in Fig. 3a. This is mainly attributed to differences in the surface properties, as described later.

The friction rate parameters are different below and above T_c (Fig. 3b). For example, α_1 is slightly greater ($7.5(2.5)\bullet10^{-5}$, below T_c) than $\alpha_0(3.7(2.1)\cdot10^{-5}$, above T_c. Also, the absolute value of β_1 is larger below than above T_c. Higher absolute values of α_1, α_0 (β_1) represent larger increments (decrements) of friction with velocity in the strengthening (weakening) regimes, while values close to zero reflect a velocity-neutral friction force. Hence, friction rate parameters are closer to zero (neutral behavior) above T_c, at both ≤ 3 and 10 % RH. In each temperature range ($<T_c$ and $>T_c$, respectively), the temperature dependence of the friction rate parameters is weak. Furthermore, the relative humidity ≤ 3 % RH vs. 10 % RH has no obvious influence on the friction rate parameters. However, the number of data points at ≤ 3 % RH is not as large as at 10 % RH, and hence, this conclusion needs to be considered with caution.

3.3. Origin of energy dissipation: Atomic stick slip friction

Representative lateral force loops at 10 % RH are shown in Fig. S8. As the temperature increases, the loop width exhibits significant variations over large sliding distances; e.g. Fig. S8l at 90 °C. Before we describe this finding, we shall examine the lateral force in flat regions of the loops over small distances. Fig. 4 shows the sawtooth profile of the lateral force at two different velocities (0.04 and 0.4 μm s^{-1}), which reflects the stick–slip motion of the tip. Indeed, the Prandtl-Tomlinson (PT) model for atomic scale friction of crystalline surfaces attributes the microscopic origin of the energy dissipation to the stick–slip motion of the tip, where the slip length depends on the dimensions of the crystal lattice [43,44].

Below 60 °C, the slip length at 0.04 μm s^{-1} is ~ 1.0–1.2 nm (indicated by the red arrow). The AFM images of calcite in aqueous solution by Rode *et al.* [45] displayed the 1 × 1 unit cell with dimension ~ 0.5 nm × 0.8 nm on the calcite's $(10\bar{1}4)$ plane at the surface. Examining this unit cell reveals a single slip length ~ 0.5 nm along the [010] direction and ~ 0.8 nm along the $[\bar{4}\bar{2}1]$ direction. In contrast, Stipp *et al.* [42] revealed the 2 × 1 unit cell at the calcite surface in contact with air. A slip length ~ 1.0–1.2 nm could imply a double slip in case of the (1 × 1) unit cell or a single slip if the (2 × 1) unit cell would be exposed. The results at other conditions support that the (1 × 1) unit cell could be present at the surface. An increase in temperature leads to smaller slip lengths, but the motion of the tip also becomes more irregular and noisier.

When the tip slides at 0.4 μm s^{-1}, the slip length is ~ 0.6–0.8 nm, and hence, closer to the single slip length for the 1 × 1 unit cell; a more irregular motion is also seen with increase of temperature. Larger slip lengths are promoted at 1 μm s^{-1} compared to 0.04 μm s^{-1} at all temperatures (~1.0–1.6 nm, Fig. S9). In contrast, the stick–slip motion is more regular at 3 % RH (Fig. S10-11), and the slip length is observed to slightly decrease with temperature from ~ 0.92 nm to ~ 0.5 nm; more details are given in the SI.

Dynamic simulations of the PT model for crystalline surfaces at low temperature (0–107 K) showed that the non-monotonic dependence of friction on velocity (first increasing and then decreasing) originates from the thermally activated slip motion, its suppression by increasing velocity, and single vs. double slips leading to different dissipation [46]. The simulations predicted that single slips evolve into double slips as velocity increases and that the probability of occurrence of single slips increases with temperature. The single slips accompany a larger energy loss per unit length compared to double slips and bring about an increase of the average frictional force. Concurrently, the sliding process is thermally activated, and hence, the average friction force decreases with

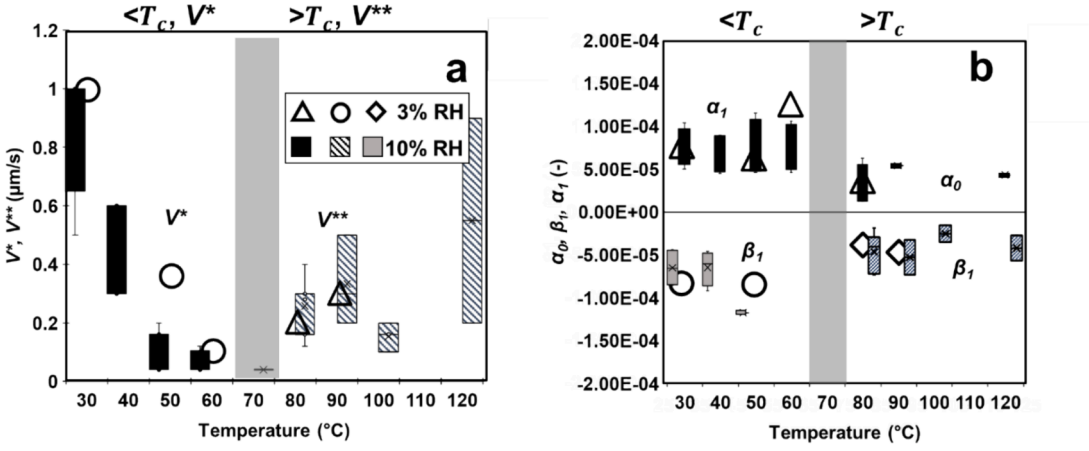

Fig. 3. Friction rate parameters and transition velocities for the velocity-dependence of the friction force. a) Transition velocities V^*, and V^{**} and b) friction rate parameters α_0, β_1 and α_1. In both Figures, the box and whisker plots correspond to 10 % RH, at which more experiments were carried out. The empty markers (circles, triangles and diamonds) represent the average values at ≤ 3 % RH; the error bars represent the standard deviation and they are smaller than the marker size and hence not visible. Friction rate parameters only at loads of 50 and 100 nN are included here. Tables S3-4 in the SI display the parameters for each load.

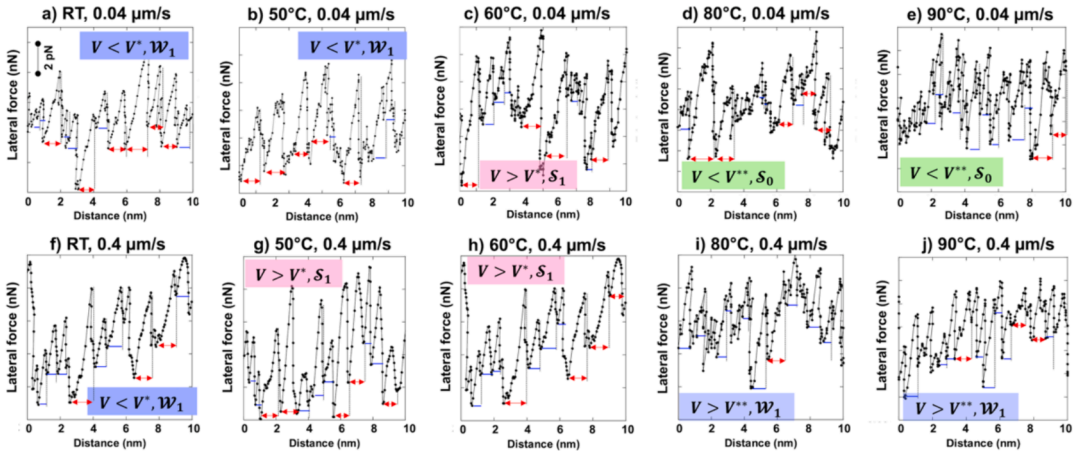

Fig. 4. Atomic stick slip. Lateral force under an applied load of 50 nN at **a;f)** room temperature, **b;g)** 50 °C, **c;h)** 60 °C, **d;i)** 80 °C, and **e;j)** 90 °C at 10 % RH. These results correspond to sliding velocities **a-e)** 0.04 and **f-j)** 0.4 μm s^{-1}. The blue solid line represents single slip (0.5–0.6 nm), while red arrows indicate the occurrence of multi-slip (>1 nm). Representative data at 1 μm s^{-1} are shown in Fig. S9. The data correspond to the results in Fig. 1 and the full lateral friction loops at these velocities are shown in Fig. S8.

increasing temperature. The competition between all these mechanisms justifies the non-monotonic dependence of friction on temperature and velocity, and the complex variation of the stick slip length. Our results are not fully consistent with these simulations, especially at 10 % RH, where there is significant irregular motion and slightly larger slip lengths at 0.04 μm s^{-1} compared to 0.4 μm s^{-1}. This suggests that the observed transitions could originate from other interfacial phenomena. As demonstrated next, the calcite surface undergoes significant changes due to hydrothermal effects and wear, which influence the frictional dissipation.

3.4. *Effects of temperature and humidity on surface topography, softness, and crystallinity*

Fig. 5 shows tapping mode AFM images of the surface of a calcite single crystal at 10 % RH, as the temperature rises from 30 to 90 °C. Tapping mode AFM allows for the simultaneous collection of height and phase-shift signals, which can resolve 3D features in the topography (height) maps while yielding real-time phase contrast maps that convey information about spatial variations of mechanical properties on the surface. For instance, elastic materials will produce an in-phase or lower phase shift response (lower angle), whilst areas with softer regions will induce a higher phase shift (higher angle). For surfaces with uniform elasticity it has been shown that increasing adhesion lead to a raise in the phase lag [47], and hence, a convolution of adhesion and mechanical properties is possible.

The images of the topography and phase of the calcite surface at 30 °C ($t_1 = 1$ h) and 40 °C ($t_2 = 2.5$ h) show terraces with atomic steps ~ 3 Å (one atomic layer). At 50 °C ($t_3 = 4$ h), a change in calcite topography is detected and rough patches with heights 2–4 Å and higher phase (~2.2°) appear on the otherwise unmodified calcite surface (Fig. 5e–f). The rough patches extend over larger areas over time at constant temperature (Fig. 5g–h, $t_4 = 4.5$ h). Previous studies at RT have shown similar morphologies on the $(10\bar{1}4)$ cleavage plane when exposed to humid air [18,19] and attributed to the local dissolution of the calcite by the adsorbed water and reprecipitation in hydrated forms of calcium carbonate like monohydrate, hexahydrate or amorphous hydrate[17]. A further increase in temperature to 60 °C (5.5 h, Fig. 5i–j) shows the surface completely covered by this rough atomic layer, with a greater thickness of 4–6 Å (up to two atomic layers), which contains darker pits with a depth of ~ 2 Å. The growth of the pits continues at 70 °C (7 h, Fig. 5k–l). At 90 °C, there is a major change of topography (Fig. 5m–n). The pits grow and coalesce with each other, leading to significant coarsening. The depth difference grows to ~ 6 Å (2 atomic layers). The atomic scale height difference leads to small RMS roughness of 175.4 pm, 423.6 and 191.6 pm at 70, 80 and 90 °C, respectively. Notably, this is concurrent with a significant increase in the phase from ~ 4° to ~ 26°. Furthermore, the change of the calcite surface is irreversible upon a decrease in temperature (Fig. S13).

Adhesion maps measured in areas 150 nm × 150 nm in function of temperature are summarized in Fig. S12. The pull-off force increases with temperature below T_c (30 ± 6 nN, 38 ± 4 nN, 57 ± 5 nN at RT, 40 °C, and 50 °C, respectively) and it decreases with a further increase in temperature to 49 ± 4 and 42 ± 4 at 60 to 80 °C, respectively. This indicates that the observed increase in phase above T_c cannot be attributed solely to adhesion, and instead, it points toward a significant surface softening.

Complementary measurements were carried out to disentangle the combined effects of humidity and temperature. First, Fig. S14 shows AFM images taken at RT after exposure to ~ 30 % RH (laboratory air) for 13 h. Rough recrystallization patches were observed after 2 h of exposure to air. They extended to the entire surface over time, indicating that a higher humidity promotes this process at RT. Lower adhesion along with increased softness on the hillocks compared to calcite terraces has been reported at RT [18]. This is consistent with the observed increase in phase after 10 h of exposure to 30 % RH in Fig. S14. Fig. S15 displays the formation of a rough atomic layer at ~ 3 % RH, while the temperature was increased. Here, the growth was much slower than at 10 % RH and many regions of the surface remained atomically smooth, while the phase (stiffness) did not significantly change with temperature.

The comparison of the calcite topography at 3, 10 % and 30 % RH supports that increasing the amount of adsorbed water promotes the roughening of the calcite surface, in agreement with previous studies at RT [17]. This is likely because at low RH there are only a few water or hydration layers strongly bound to the surface [8,9,18,19,48,49], which limits the dissolution of calcite. In addition, the adsorbed water is often termed “ice-like” due to the slow dynamics, which should greatly hinder mass transfer. The diffusion coefficient of ions in hydration layers can be 1 to 2 orders of magnitude smaller than the diffusion coefficient in bulk water [48]. Hence, the observed dissolution-reprecipitation process might become diffusion-limited at sufficiently small relative humidity. It is also evident that increasing temperature promotes the roughening and softening of the calcite surface at 10 % RH. Although the solubility of calcite decreases with temperature, dissolution, diffusion and precipitation are thermally activated processes –i.e. the rate constants are Arrhenius-type– which supports that higher temperature may accelerate the kinetics of the calcite surface reconstruction [50,51].

High temperature X-ray diffraction (HT-XRD) was used to examine

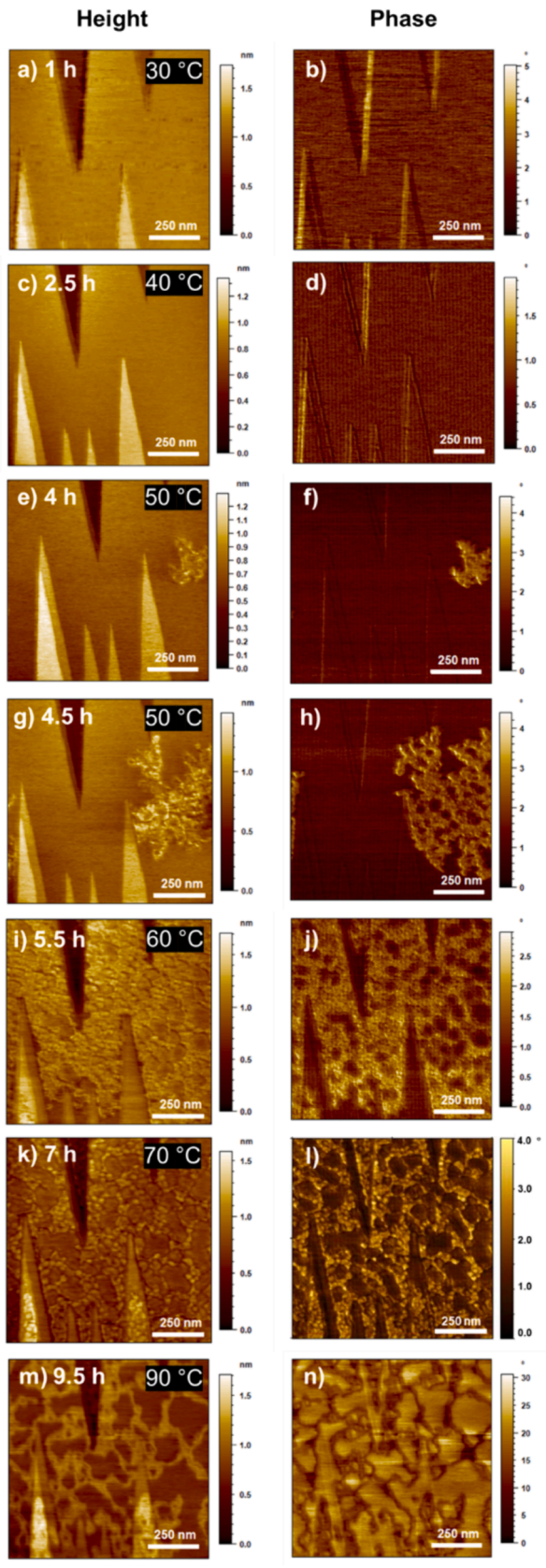

Fig. 5. AFM topographical and phase images of calcite. The images were taken at **a-b)** 30 °C, **c-d)** 40 °C, **e-h)** 50 °C, **i-j)** 60 °C, **k-l)** 70 °C, and **m-n)** 90 °C at 10 % RH. AFM images were taken in tapping mode with a sharp tip on the same calcite single crystal at all temperatures. The thermal drift is enhanced with temperature and is responsible for the small shift of the imaged area.

the crystallinity of cleaved calcite crystals. HT-XRD consistently showed a decrease in crystallinity (i.e., from 92.2 % to 87.4 %) upon a temperature increase from 25 °C to 150 °C in Argon atmosphere, i.e., calcite became slightly more amorphous with increase in temperature (Fig. S16). There is also a small expansion of the crystal lattice inferred from the shift of the diffraction peaks corresponding to (104), (110), (018) and (116) planes. Thermal expansion of the crystal lattice has been reported before for calcite(Markgraf & Reeder, 1985) at T > 200 °C [52–54], but here, we investigated lower temperatures. The reduction in crystallinity of pre-heated calcite was confirmed by room temperature XRD (Fig. S17). These results indicate that the softening of the calcite surface above 60 °C inferred from AFM images may be, at least partially, due to the thermal expansion of the crystal lattice and its amorphization.

While the changes in topography, adhesion and elasticity must influence the friction force, it is to be noted that AFM imaging takes a bit longer than friction measurements at each temperature (1.5 h vs. 1 h), and hence, the change of the calcite surface during friction measurements could be a bit less significant. Note that the softening of the calcite surface coincides with the onset of the $\mathscr{S}_0$ regime.

3.5. Wear of the calcite surface

In wear tests, the tip slid over a small area on the freshly cleaved calcite surface (white box in Fig. 6) from the left to the right (trace) and in the reverse direction (retrace) applying a high load (100 nN, 0.69 GPa). This was repeated ten times (scans) to simulate the conditions of the friction measurements, but over a square area instead of a line; see Methods section. Fig. 6 shows images of the calcite surfaces before and after wear measurements at RT, 50 and 90 °C and three sliding velocities, 0.2, 1 and 10 μm s^{-1}. The friction regime corresponding to each condition is displayed in each image. At RT, 0.2 μm s^{-1} falls in the $\mathscr{W}_1$ regime, while 10 μm s^{-1} corresponds to the $\mathscr{S}_1$ regime, and 1 μm s^{-1} falls at the transition. At 50 °C, 0.2, 1 and 10 μm s^{-1} fall in the $\mathscr{S}_1$ regime. At 90 °C, 1 and 10 μm s^{-1} fall in the $\mathscr{W}_1$ regime, while 0.2 μm s^{-1} is at the transition between $\mathscr{S}_0$ and $\mathscr{W}_1$ regimes. Fig. 6 only displays the smooth calcite surface at RT before wear measurements, but the surface was initially equally smooth at all temperatures.

Pits formed at RT and 0.2 μm s^{-1}, they became larger and merged upon repeated sliding. Complementary images illustrating the growth of the pits are displayed in Fig. S18. Three layers of calcite (~9 Å) were removed at 0.2 μm s^{-1}, whereas no wear was observed at 1 and 10 μm s^{-1} at RT. Increasing temperature to 50 °C promoted wear, as visible pits of ~ 9 Å in depth are observed at 0.2 and 1 μm s^{-1}. At 80 °C, a wear track was observed at all sliding velocities, but the depth was greater with a decrease in velocity and there were no signs of pit formation. Indeed, the images suggest that the tip pushes the atomic layers to the right and left sides of the wear track, where the height increases; this suggests that the tip removes material through plowing. These images let us hypothesize that the observed softening above T_c promotes wear of the calcite surface. Reducing the relative humidity to < 3 % RH results in a significant decrease in wear (Fig. S19), which suggests that hygrothermal effects -i.e. the dissolution–recrystallization of the calcite surface and its softening- promote the removal of the surface layers. This is also consistent with our previous study at RT and 0 % RH, where atomic attrition was hypothesized to lead to pit formation on calcite at a contact stress of ~ 0.75 GPa [29], very close to the stress applied here. It is thus evident that a moderate humidity of 10 % RH significantly enhances wear at all temperatures, but more so above T_c.

3.6. Hygrothermal effects on surface structure

Prior works have thoroughly investigated the spontaneous formation of hillocks and pits on terraces and steps on the calcite surface when exposed to air at RT [8,17–19,21,42,55–57]. In general, higher humidity induces faster reconstruction of the surface. For instance, hillocks were observed after 4 h at 25 % RH, while it only took ~ 2 h above 50 % RH,

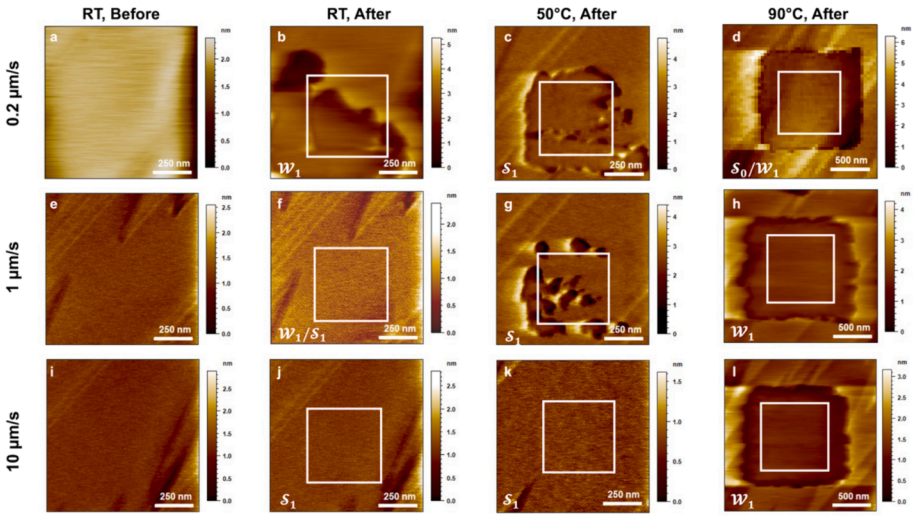

Fig. 6. Nanoscale wear measurements at ~ 10 % RH and various temperatures (RT, 50 and 90 °C). Contact mode images (1 μm × 1 μm) were taken under an applied load of 5 nN (low load) before wear measurements (labelled as "before"). Then, ten contact mode images were taken while the tip slid within the white square (0.5 μm × 0.5 μm) at **a-d)** 0.2 μm s^{-1}, **e-h)** 1 μm s^{-1}, and **i-l)** 10 μm s^{-1}. The contact pressure was similar to that applied with the tip at 50 nN in Figs. 1 and 2, Contact mode images (1 μm × 1 μm) labeled "after" were taken at low load (5 nN) to visualize the wear footprint. The instrument drift leads to the motion of the calcite surface during the wear tests and is presumably the reason why the wear track is larger than the white square.

as reported by Wojas *et al.* [18]. This is consistent with our results at < 3 % RH vs. 10 % RH vs. 30 % RH. Four different types of behavior were identified by Stipp *et al.* [8]. One of them, the least ordered growth of hillocks, was attributed to the rapid accumulation of material, which sometimes also rapidly disappeared at some spots, leaving large holes. The hillocks developed in a flower shape, and the fresh surface was covered completely with 4–10 monolayers of calcium carbonate within 30 min at 30 % RH. The morphology reported was, indeed, similar to that displayed in Fig. 5m–n, yet this morphology is observed at lower RH and higher temperature in our study. Furthermore, the thickness of the re-precipitated layers is up to ~ 6 Å (~2 calcium carbonate monolayers). Interestingly, a similar height of hillock clusters (6.4 ± 0.9 to 7.6 ± 1.9 Å) was reported by Wojas *et al.* above 25 % RH at RT [18]. Hillocks and pits were shown to spread after reaching a stable height, yet the surface coverage did not exceed 25 %. Instead, our images display a much higher surface coverage at 60 °C (5.5 h) and 70 °C (7 h) even though the humidity was much smaller. Analogously, only trench-like clusters were detected < 3 % RH by Wojas *et al.*, while both hillocks and trenches are observed in our studies at higher temperature. Overall, the faster reconstruction in our experiments can be justified by the thermal activation of dissolution and precipitation, and higher diffusivity, as the temperature increases.

Two models have been put forward in the literature to explain the reconstruction of the calcite surface at RT. The first one assumes the water layer has a constant height of 15 Å with a low-density (~0.1 g/cm^3) region close to the surface, whose thickness increases from 0.6 to 2 Å with RH; and a capillary region with density increasing from 0.6 to 0.9 g/cm^3 with RH [16,19]. The second one suggests the thickness of the water layer is limited to a single monolayer (~3 Å) at low humidity and it evolves to multiple monolayers at higher humidity [22]. Our results show the reconstructed layer thickness increases from ~ 3 Å to ~ 6 Å with increasing temperature at ~ 10 % RH, despite the decrease of calcite solubility. This cannot be reconciled with an increase in the number of adsorbed water layers at higher temperature, but it can be presumably attributed to the smaller atomic density (greater volume) of the precipitated calcite layer, as inferred from the much softer surface of calcite and the lower crystallinity. This points toward the formation of amorphous hydrate calcite carbonate on the calcite surface [17].

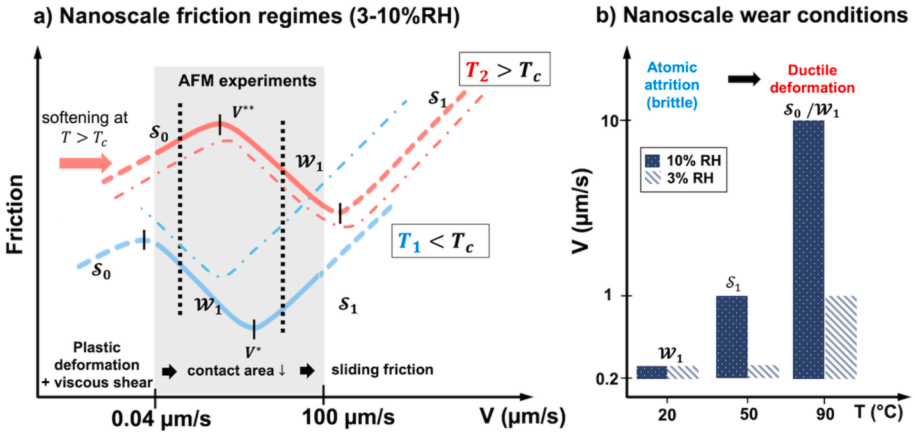

Fig. 7. A) Friction-velocity plot showing transitions of friction regimes below T_c (blue solid line) and above T_c (red solid line). The dot-dashed curves are friction-velocity curves at higher temperature below T_c and above T_c, respectively. The investigated velocity range (0.04 to 100 μm s^{-1}) is marked in grey. Transitions from $\mathscr{S}_1$ to $\mathscr{W}_1$ and from $\mathscr{W}_1$ to $\mathscr{S}_0$ are observed with increase in temperature at high and low sliding velocity, respectively; see dashed vertical lines. **b)** Summary of velocity and temperature conditions where visible wear occurs at ≤ 3 % RH (solid) and 10 % RH (patterned) under an applied load of 100 nN (0.57–0.69 GPa).

3.7. Temperature-dependent mechanisms of friction and wear

Fig. 7a summarizes the results from our friction measurements at 10 % RH. We posit that the isothermal frictional characteristics of calcite exhibit transitions from $\mathscr{S}_0$ to $\mathscr{W}_1$ to $\mathscr{S}_1$ regimes with an increase in velocity. The range of accessible sliding velocities with our AFM does not let us probe the $\mathscr{S}_0$-regime below T_c. However, an increase in temperature above T_c shifts the friction-velocity curve to the right, so that the velocity-strengthening friction ($\mathscr{S}_0$) regime can be probed at slow sliding velocities (below V^{**}). Fig. 7b summarizes the temperature and velocity conditions at which wear of calcite happens under the same conditions. Wear is observed in $\mathscr{S}_0$, $\mathscr{W}_1$ and $\mathscr{S}_1$ regimes, but it is enhanced above T_c and at 10 % RH. This is presumably attributed to the hygrothermal changes of the calcite surface and to the influence of temperature on dislocation plasticity; for calcite, it is 10^6-10^8 times faster at 80 °C compared to 18 °C [58].

In the $\mathscr{S}_0$-regime, the tip slides very slowly along the calcite surface. Prompted by the significant softening of the reconstructed calcite surface above T_c, the tip may plastically deform the surface and abrade the surface layers. The softening of the calcite surface is believed to be the main mechanism responsible for the shift of the friction-velocity curve to the right at T_c. As velocity increases, both the abrasion (plowing) of the surface as well as the contact area between calcite and the tip decrease, leading to velocity-weakening friction ($\mathscr{W}_1$). Their competition with the viscous shear leads to the transition at V^{**} from $\mathscr{W}_1$ to $\mathscr{S}_0$ as velocity decreases. It is evident that the atomic scale reconstruction of the surface, its remarkable softening (facilitating the displacement of the atoms by the tip or plowing) and the decreasing crystallinity must impair the regular stick–slip motion of the tip, thereby justifying the irregular slip length at high temperature.

Below T_c, the surface is assumed to behave more elastic, and velocity-weakening friction is justified by contact ageing as a result of atomic attrition, as we invoked at 0 % RH [29]. However, that previous work showed a much less prominent surface damage of calcite. Based on this, we believe that the enhancement of wear at 10 % RH is related to the pressure-induced dissolution of calcite. During pressure solution, the confined fluid becomes undersaturated with respect to the stressed mineral, which induces its dissolution. The dissolved ions diffuse and precipitate in adjacent regions, where the solution is supersaturated, while the tip slides away. Hence, it is possible that the pressure-induced dissolution of calcite is, at least, partially responsible for pit enhancement, especially at low temperature, at which the solubility of calcite is greater. As the velocity further increases, the competition between these mechanisms and nanoscale sliding friction (also referred to as shear-assisted thermally activated slip in the context of the classical PT model [43,44]) leads to the second transition from $\mathscr{W}_1$ to $\mathscr{S}_1$ at V^*.

The proposed dissipation mechanisms are also valid at $\leq$ 3 % RH, albeit there are differences with respect to the results at 10 % RH. Indeed, instead of the $\mathscr{S}_0$ regime, friction remains approximately constant at elevated temperature and slow sliding (Fig. S7). This is attributed to the less significant reconstruction and softening of the calcite surface, and thereby also reduced wear at 3 % RH compared to 10 % RH. We note that a previous study compared friction and wear at $<$ 5 % and 75 % RH at RT and showed that the presence of water significantly reduced wear [38], in contrast to our results at 10 % RH. Although the amplitude of the stick–slip indicated that the surface becomes softer and less brittle at 75 %RH, the action of capillary forces was suggested to retain the wear particles in the wear track and thereby lead to the reduction of abrasive wear. The much lower humidity in our work prevents the action of capillary forces.

The influence of the temperature is also relevant below and above T_c, respectively; see dot-dashed lines in Fig. 7a. Increasing the temperature —above T_c— leads to an increase of V^{**}, and hence, it shifts this curve to the right and the $\mathscr{S}_0$ regime extends over a slightly wider range of velocities with increase in temperature. The decrease in friction with temperature in $\mathscr{S}_0$ and $\mathscr{W}_1$ regimes is consistent with the thermal activation of the underlying mechanisms. Increasing the temperature —yet below T_c— shifts the friction-velocity curve to the left, as V^* is observed to decrease (Fig. 3), so that the $\mathscr{S}_1$ regime extends over a wider range of velocities. Here, friction is seen to increase with temperature, which is more intriguing; see Fig. S20. The increasing adhesion and roughness as reconstruction happens, and the more numerous single slips may account for this increase. Note that roughness was also shown to cause both the extension of the velocity-strengthening regime and an increase in friction at 0 % RH and RT, in our previous work [29].

3.8. Comparison to nanoscale studies on other crystals at low T and proposed mechanisms

Non-monotonic trends of friction in function of velocity and temperature have been reported for other crystals, such as NaCl (111) and Si (111) probed by naturally oxidized Si tips in UHV [59,60]. For example, NaCl(111) exhibits a friction peak at a cryogenic temperature ~ -103 °C. The simulations by Mazo *et al.* [61] using an extended PT model were able to reproduce the friction peak for NaCl (111). The averaged static force followed a similar trend as displayed in Fig. 7a, with a less steep and narrow $\mathscr{S}_1$ regime that was not examined, as sliding velocities were smaller than in this work. The experiments showed that the lateral stiffness, and thereby the contact area, decreased logarithmically with the velocity up to a saturation value and associated this change with the pressure-induced surface diffusion of single atoms in the contact, which led to wear by atomic attrition. This led to an increase of the friction force with velocity up to a certain value, where the effect of thermally activated slip was superseded by contact ageing and the slope of friction vs. velocity was reversed. As the temperature increased from 100 K to 300 K, the static friction force shifted gradually to the right, causing the slope reversal in the velocity dependence -from velocity-weakening (below T_c) and velocity-strengthening friction (above T_c). Importantly, the surface properties of NaCl remained constant at UHV and low temperatures, in great contrast to the results for calcite, greatly simplifying the underlying mechanisms.

A multibond model [62] was also able to reproduce the peak in friction at a cryogenic temperature (T_{max}) for Si(111), as well as the velocity-weakening friction below T_{max} and velocity-strengthening friction above T_{max}, while neglecting atomic attrition; T_{max} corresponds to T_c in this work. This model considers the friction peak results from two competing processes acting at the interface: the thermally activated formation and rupturing of the attachment of atomic contacts. This is different from the Prandtl-Tomlinson model, where the distance traversed by the tip during sliding is determined by the periodicity of the surface potential. In the multibond model, it is defined by the interplay between the rupture and reattachment rates. The stick–slip motion of the tip below T_c thus results from the cooperative behavior of atomic contacts. Above T_c, when the reattachment rate approaches the rate of force relaxation close to the peak, the stick–slip motion becomes more and more irregular, as we also observed. However, the frictional characteristics (especially at 10 % RH) cannot be simply attributed to the (re) attachment rates and we claim that the hygrothermal effects on the $(10\bar{1}4)$ plane of calcite surface is responsible for the reported complexity.

Similarly, friction measurements on Si (100) with a native SiO_2 layer using a Si_3N_4 tip at 50 %RH and RT showed velocity-weakening (like $\mathscr{W}_1$) followed by velocity-strengthening friction (like $\mathscr{S}_1$) [63]. The authors claimed that the meniscus formed at the interface due to the high humidity and the induced tribochemical reaction -i.e. the formation of a low shear strength $Si(OH)_4$ layer- were responsible for the weakening regime. Interestingly, the authors attributed the velocity-strengthening friction to asperity deformation. The RMS roughness of the native silicon oxide layer is ~ 1 nm [64,65], and hence, similar to that of the $(10\bar{1}4)$ plane of calcite upon dissolution/reprecipitation.

Note that multi-asperity contacts were assumed in that work, while a single-asperity contact represents better our contact geometry; see Fig. S21. However, we do agree that plastic deformation could contribute to frictional dissipation, especially at small sliding velocities (longer contact time, larger deformation), and higher temperature.

3.9. Comparison to macroscale geophysical studies at high T

There is intense research on characterizing the frictional properties of fault gouge materials in macroscale experiments due to its significance for fault dynamics and earthquake nucleation. Similar to the change in the velocity-dependence of friction at $T_c \sim 70$ °C at the nanoscale, Verberne *et al.* reported a transition from velocity-strengthening friction to velocity-weakening friction for dry limestone gouge at ~ 70–100 °C [58,66,67]; the main constituent of limestone is calcite. For dry carbonate fault breccia-derived samples, Chen *et al.* observed this transition at 80 °C [68]. The transition was suggested to be controlled by the competition between crystal plasticity and granular flow processes. While the transitional behavior is observed at a temperature close to T_c, granular flow is excluded in our AFM experiments, and hence, our work reveals alternative or complementary mechanisms to justify this macroscopic behavior.

Furthermore, the velocity-weakening friction for calcite gouge has been often associated with the compaction induced by solution transfer processes like pressure solution [69,70]. This phenomenon is proposed to promote grain compaction (sometimes cementation), and thereby, causes an increase in friction at slower sliding velocities [69,71]. In a similar AFM set-up to the one used here, our studies of pressure solution in liquid environment did not show any compaction or cementation, presumably because the tip slides away and the mineral precipitates outside the contact area [27]. Instead, we showed that friction decreases with an increase in pressure; labelled as pressure solution facilitated slip. Moreover, friction was shown to increase linearly with sliding velocity during pressure solution in liquid environment [29]. This seemingly contradictory phenomena, yet at disparate length scales, calls for a careful revision of the relation between nano- and macroscale calcite friction, which will be discussed in a separate work.

When compared to our previous studies in aqueous solution, a decrease in friction with load or pressure did not happen at 3–10 % RH, and friction did not increase linearly with sliding velocity, either. Hence, we can exclude the relevance of pressure solution facilitated slip in the nanoscale frictional characteristics of calcite at low humidity. However, we cannot exclude that pressure solution happens and this tribochemical phenomenon influences wear and friction, as discussed earlier.

4. Conclusion

This work presents the nanoscale investigation of the influence of temperature on the tribochemical characteristics of calcite in a low humidity environment. The dissolution/re-precipitation of the calcite surface occurs in agreement with previous observations and models [8,18,20,42]. However, the coverage and thickness of hillocks and pits is enhanced with an increase in temperature, consistent with the thermal activation of dissolution and re-precipitation and faster diffusion, despite the decrease in calcite solubility. In addition to that, a major softening of the surface happens above $T_c \sim 70$ °C. Furthermore, all these processes are enhanced at 10 % RH compared to 3 % RH, and hence, in presence of more water. The influence of the temperature on friction is intricate. The friction-velocity profile exhibits three logarithmic regimes with distinct dominating mechanisms: a velocity-strengthening friction ($\mathscr{S}_0$) at $V < V^{**}$; a weakening regime $\mathscr{W}_1$ ($V^{**} < V < V^{*}$); and a second strengthening regime $\mathscr{S}_1$ at $V > V^{*}$. An increase of temperature above T_c, shifts the friction-velocity curve to the right, and enables to probe $\mathscr{S}_0$ and $\mathscr{W}_1$ regimes by AFM, while $\mathscr{W}_1$ and $\mathscr{S}_1$ regimes are probed below T_c within the same range of velocities. As a result of this behavior, the friction force exhibits an abrupt transition at T_c; friction increases (decreases) with temperature below (above) T_c. This reflects the action of different underlying dissipation mechanisms. Meanwhile, the abrasive wear of calcite is more significant above T_c and at 10 % RH.

The comparison of the interfacial, friction and wear results helps elucidate the underlying mechanisms and reflects the crucial role of the water molecules at the mineral surface. We propose that $\mathscr{S}_1$ results from the thermal activated slip within the scope of the PT model or its extensions, while $\mathscr{W}_1$ reflects contact ageing due to atomic attrition at low T. Previous nanoscale studies have proposed similar mechanisms for other materials at UHV [59–61,72]. For calcite at 10 % RH, however, pressure-induced dissolution plays a role by enhancing pit formation and roughness. The significant reconstruction and softening of the calcite surface above T_c enable to resolve $\mathscr{S}_0$ at slow sliding velocities and 10 % RH, which is proposed to originate from plastic deformation and viscous shear. Furthermore, the increase in temperature thus leads to wear by (plowing) abrasion, while pressure-induced dissolution of calcite could be at play, as well. Lowering the RH to ~ 3 %, mitigates surface reconstruction, pressure-induced dissolution, softening, causing the $\mathscr{S}_0$ regime to be less prominent and reducing wear.

The findings from this study are relevant to several geological and industrial processes. Studies of the thermal effects on calcite friction and wear in aqueous environment are required to extend this knowledge to the calcite/solution interface, e.g. thermal effects on pressure solution and its influence on friction. AFM measurements at calcite-calcite contacts are under way to examine the influence of the composition of the countersurface, e.g. on potential cementation. Simulations could complement experimental studies to provide insight into the underlying mechanisms and we hope to capture attention through this work. Microscale studies with surface force apparatus [36,37,73,74] or similar instruments can help narrow the gap in understanding the relation between nano- and macroscale phenomena and should be considered for future tribological studies, as well.

CRediT authorship contribution statement

Binxin Fu: Writing – review & editing, Writing – original draft, Visualization, Methodology, Investigation, Formal analysis, Conceptualization. **Rosa M. Espinosa-Marzal:** Writing – review & editing, Writing – original draft, Visualization, Validation, Supervision, Funding acquisition, Formal analysis, Conceptualization.

Declaration of competing interest

The authors declare that they have no known competing financial interests or personal relationships that could have appeared to influence the work reported in this paper.

Data availability

Data will be made available on request.

Acknowledgments

This work was supported by the National Science Foundation Grant number EAR-1856525.

Appendix A. Supplementary data

Supplementary data to this article can be found online at https://doi.org/10.1016/j.jcis.2024.03.035.

References

[1] H.A. Lowenstam, Factors affecting the aragonite: calcite ratios in carbonate-secreting marine organisms, J. Geol. 62 (3) (1954) 284–322.
[2] E. Liteanu, C.J. Spiers, Influence of pore fluid salt content on compaction creep of calcite aggregates in the presence of supercritical CO_2, Chem. Geol. 265 (1–2) (2009) 134–147.
[3] T.P. Burchette, Carbonate rocks and petroleum reservoirs: a geological perspective from the industry, Geol. Soc. Lond. Spec. Publ. 370 (1) (2012) 17–37.
[4] R. Han, T. Shimamoto, T. Hirose, J.H. Ree, J. Ando, Ultralow friction of carbonate faults caused by thermal decomposition, Sci. 316 (5826) (2007) 878–881.
[5] F.W. Tegethoff, J. Rohleder, E. Kroker, Calcium carbonate: from the cretaceous period into the 21st century, Springer Science & Business Media, 2001.
[6] F. Heberling, T.P. Trainor, J. Lutzenkirchen, P. Eng, M.A. Denecke, D. Bosbach, Structure and reactivity of the calcite-water interface, J Colloid Interf Sci 354 (2) (2011) 843–857.
[7] Y. Diao, R.M. Espinosa-Marzal, Molecular insight into the nanoconfined calcite–solution interface, Proc. Natl. Acad. Sci. 113 (43) (2016) 12047–12052.
[8] S.L.S. Stipp, W. Gutmannsbauer, T. Lehmann, The dynamic nature of calcite surfaces in air, Am Mineral 81 (1–2) (1996) 1–8.
[9] S.L.S. Stipp, Toward a conceptual model of the calcite surface: hydration, hydrolysis, and surface potential, Geochim. Cosmochim. Acta 63 (19–20) (1999) 3121–3131.
[10] P. Fenter, P. Geissbühler, E. DiMasi, G. Srajer, L. Sorensen, N. Sturchio, Surface speciation of calcite observed in situ by high-resolution X-ray reflectivity, Geochim Cosmochim Ac 64 (7) (2000) 1221–1228.
[11] F. Heberling, D. Bosbach, J.-D. Eckhardt, U. Fischer, J. Glowacky, M. Haist, U. Kramar, S. Loos, H.S. Müller, T. Neumann, Reactivity of the calcite–water-interface, from molecular scale processes to geochemical engineering, Appl. Geochem. 45 (2014) 158–190.
[12] P. Fenter, S. Kerisit, P. Raiteri, J.D. Gale, Is the calcite–water interface understood? direct comparisons of molecular dynamics simulations with specular X-ray reflectivity data, J. Phys. Chem. C 117 (10) (2013) 5028–5042.
[13] D.W. Thompson, P.G. Pownall, Surface electrical properties of calcite, J. Colloid Interface Sci. 131 (1) (1989) 74–82.
[14] N. de Leeuw, S. Parker, Atomistic simulation of the effect of molecular adsorption of water on the surface structure and energies of calcite surfaces, J. Chem. Soc. Faraday Trans. 93 (3) (1997) 467–475.
[15] S. Stipp, J. Konnerup-Madsen, K. Franzreb, A. Kulik, H. Mathieu, Spontaneous movement of ions through calcite at standard temperature and pressure, Nature 396 (6709) (1998) 356–359.
[16] P. Geissbühler, P. Fenter, E. DiMasi, G. Srajer, L. Sorensen, N. Sturchio, Three-dimensional structure of the calcite–water interface by surface X-ray scattering, Surf. Sci. 573 (2) (2004) 191–203.
[17] P.M. Claesson, N.A. Wojas, R. Corkery, A. Dedinaite, J. Schoelkopf, E. Tyrode, The dynamic nature of natural and fatty acid modified calcite surfaces, Phys. Chem. Chem. Phys. 26 (4) (2024) 2780–2805.
[18] N.A. Wojas, A. Swerin, V. Wallqvist, M. Jarn, J. Schoelkopf, P.A.C. Gane, P. M. Claesson, Iceland spar calcite: humidity and time effects on surface properties and their reversibility, J. Colloid Interf Sci. 541 (2019) 42–55.
[19] J. Bohr, R.A. Wogelius, P.M. Morris, S.L.S. Stipp, Thickness and structure of the water film deposited from vapour on calcite surfaces, Geochim. Cosmochim. Acta 74 (21) (2010) 5985–5999.
[20] S.L. Stipp, M.F. Hochella Jr, G.A. Parks, J.O. Leckie, Cd2+ uptake by calcite, solid-state diffusion, and the formation of solid-solution: Interface processes observed with near-surface sensitive techniques (XPS, LEED, and AES), Geochim Cosmochim Ac 56 (5) (1992) 1941–1954.
[21] A. Rahaman, V.H. Grassian, C.J. Margulis, Dynamics of water adsorption onto a calcite Surface as a function of relative humidity, J. Phys. Chem. C 112 (6) (2008) 2109–2115.
[22] T.A. Kendall, S.T. Martin, Mobile ions on carbonate surfaces, Geochim Cosmochim Ac 69 (13) (2005) 3257–3263.
[23] N. Fernandez, J. Cayer-Barrioz, L. Isa, N.D. Spencer, Direct, robust technique for the measurement of friction between microspheres, Langmuir 31 (32) (2015) 8809–8817.
[24] M.A. Hubbe, R.A. Gill, Fillers for papermaking: a review of their properties, usage practices, and their mechanistic role, BioResources 11 (1) (2016) 2886–2963.
[25] Q. Li, T.E. Tullis, D. Goldsby, R.W. Carpick, Frictional ageing from interfacial bonding and the origins of rate and state friction, Nature 480 (7376) (2011) 233–236.
[26] K. Tian, N.N. Gosvami, D.L. Goldsby, Y. Liu, I. Szlufarska, R.W. Carpick, Load and time dependence of Interfacial chemical bond-induced friction at the nanoscale, Phys. Rev. Lett. 118 (7) (2017) 076103.
[27] Y. Diao, R.M. Espinosa-Marzal, The role of water in fault lubrication, Nat Commun 9 (1) (2018) 2309.
[28] Y. Diao, R.M. Espinosa-Marzal, Effect of fluid chemistry on the interfacial composition, adhesion, and frictional response of calcite single crystals—implications for injection-induced seismicity, J. Geophys. Res. Solid Earth 124 (6) (2019) 5607–5628.
[29] B. Fu, R.M. Espinosa-Marzal, Velocity-weakening and-strengthening friction at single and multiasperity contacts with calcite single crystals, Proc. Natl. Acad. Sci. U.S.A. 119 (22) (2022) e2112505119.
[30] C.M. Mate, G.M. McClelland, R. Erlandsson, S. Chiang, Atomic-scale friction of a tungsten tip on a graphite surface, Scanning Tunneling Microscopy (1993) 226–229.
[31] E. Gnecco, E. Meyer, Fundamentals of friction and Wear on the nanoscale, Springer, 2015.
[32] C.M. Mate, R.W. Carpick, Tribology on the small scale: a modern textbook on friction, lubrication, and wear, Oxford graduate texts2019.
[33] N.S. Park, M.W. Kim, S. Langford, J. Dickinson, Atomic layer wear of single-crystal calcite in aqueous solution using scanning force microscopy, J. Appl. Phys. 80 (5) (1996) 2680–2686.
[34] J. Dickinson, N.-S. Park, M.-W. Kim, S. Langford, A scanning force microscope study of a tribochemicalsystem: stress-enhanced dissolution, Tribol. Lett. 3 (1) (1997) 69–80.
[35] N.-S. Park, M.-W. Kim, S. Langford, J. Dickinson, Tribological enhancement of CaCO3 dissolution during scanning force microscopy, Langmuir 12 (19) (1996) 4599–4604.
[36] B. Fu, Y. Diao, R.M. Espinosa-Marzal, Nanoscale insight into the relation between pressure solution of calcite and interfacial friction, J Colloid Interf Sci. 601 (2021) 254–264.
[37] Y. Diao, A. Li, R.M. Espinosa-Marzal, Ion specific effects on the pressure solution of calcite single crystals, Geochim. Cosmochim. Acta 280 (2020) 116–129.
[38] N.A. Wojas, I. Dobryden, V. Wallqvist, A. Swerin, M. Jarn, J. Schoelkopf, P.A. C. Gane, P.M. Claesson, Nanoscale Wear and mechanical properties of calcite: effects of Stearic acid modification and water vapor, Langmuir 37 (32) (2021) 9826–9837.
[39] J.L. Hutter, J. Bechhoefer, Calibration of atomic-force microscope tips, Rev. Sci. Instrum. 64 (7) (1993) 1868–1873.
[40] N. Mullin, J.K. Hobbs, A non-contact, thermal noise based method for the calibration of lateral deflection sensitivity in atomic force microscopy, Rev. Sci. Instrum 85 (11) (2014) 113703.
[41] T.D.B. Jacobs, R.W. Carpick, Nanoscale wear as a stress-assisted chemical reaction, Nat. Nanotechnol. 8 (2) (2013) 108–112.
[42] S. Stipp, C. Eggleston, B. Nielsen, Calcite surface structure observed at microtopographic and molecular scales with atomic force microscopy (AFM), Geochim. Cosmochim. Acta 58 (14) (1994) 3023–3033.
[43] L. Prandtl, Ein gedankenmodell zur kinetischen theorie der festen körper, Z Angew Math Mech. 8 (2) (1928) 85–106.
[44] G.A. Tomlinson, CVI. a molecular theory of friction, Lond. Edinb. Dublin Philos. Mag. J. Sci. 7 (46) (1929) 905–939.
[45] S. Rode, N. Oyabu, K. Kobayashi, H. Yamada, A. Kuhnle, True atomic-resolution imaging of (1014) calcite in aqueous solution by frequency modulation atomic force microscopy, Langmuir 25 (5) (2009) 2850–2853.
[46] J. Nakamura, S. Wakunami, A. Natori, Double-slip mechanism in atomic-scale friction: tomlinson model at finite temperatures, Phys. Rev. B 72 (23) (2005) 235415.
[47] A. Noy, C.H. Sanders, D.V. Vezenov, S.S. Wong, C.M. Lieber, Chemically-sensitive imaging in tapping mode by chemical force microscopy: relationship between phase lag and adhesion, Langmuir 14 (7) (1998) 1508–1511.
[48] S. Kerisit, S.C. Parker, Free energy of adsorption of water and metal ions on the [1014] calcite surface, J. Am Chem. Soc 126 (32) (2004) 10152–10161.
[49] T.D. Perry IV, R.T. Cygan, R. Mitchell, Molecular models of a hydrated calcite mineral surface, Geochim. Cosmochim. Acta 71 (24) (2007) 5876–5887.
[50] J.D. Naviaux, A.V. Subhas, N.E. Rollins, S. Dong, W.M. Berelson, J.F. Adkins, Temperature dependence of calcite dissolution kinetics in seawater, Geochim. Cosmochim. Acta 246 (2019) 363–384.
[51] A. Gutjahr, H. Dabringhaus, R. Lacmann, Studies of the growth and dissolution kinetics of the CaCO3 polymorphs calcite and aragonite I. growth and dissolution rates in water, J. Cryst. Growth 158 (3) (1996) 296–309.
[52] K.V.K. Rao, S.V.N. Naidu, K.S. Murthy, Precision lattice parameters and thermal expansion of calcite, J. Phys. Chem. Solid 29 (2) (1968) 245–248.
[53] L. Tao, Z. Li, G.-C. Wang, B.-Y. Cui, X.-T. Yin, Q. Wang, Evolution of calcite surface reconstruction and interface adsorption of calcite-CO2 with temperature, Mater. Res. Express. 6 (2) (2018) 025035.
[54] J.L. Rosenholtz, D.T. Smith, Linear thermal expansion of calcite, Var Iceland Spar, and Yule Marble, Am Mineral 34 (11–1) (1949) 846–854.
[55] J. Baltrusaitis, V.H. Grassian, Calcite ($10\bar{1}4$) surface in humid environments, Surf. Sci. 603 (17) (2009) L99–L104.
[56] P. López-Arce, L.S. Gómez-Villalba, S. Martínez-Ramírez, M.Á. De Buergo, R. Fort, Influence of relative humidity on the carbonation of calcium hydroxide nanoparticles and the formation of calcium carbonate polymorphs, Powder Technol. 205 (1–3) (2011) 263–269.
[57] U. Magdans, H. Gies, X. Torrelles, J. Rius, Investigation of the {104} surface of calcite under dry and humid atmospheric conditions with grazing incidence X-ray diffraction (GIXRD), Eur. J. Mineral. 18 (1) (2006) 83–92.
[58] B.A. Verberne, J.H. de Bresser, A.R. Niemeijer, C.J. Spiers, D.M. de Winter, O. Plümper, Nanocrystalline slip zones in calcite fault gouge show intense crystallographic preferred orientation: crystal plasticity at sub-seismic slip rates at 18–150 C, Geology 41 (8) (2013) 863–866.
[59] I. Barel, M. Urbakh, L. Jansen, A. Schirmeisen, Temperature dependence of friction at the nanoscale: when the unexpected turns normal, Tribol. Lett. 39 (3) (2010) 311–319.
[60] I. Barel, M. Urbakh, L. Jansen, A. Schirmeisen, Unexpected temperature and velocity dependencies of atomic-scale stick-slip friction, Phys. Rev. B 84 (11) (2011) 115417.
[61] J.J. Mazo, D. Dietzel, A. Schirmeisen, J.G. Vilhena, E. Gnecco, Time strengthening of crystal nanocontacts, Phys. Rev. Lett. 118 (24) (2017) 246101.
[62] I. Barel, M. Urbakh, L. Jansen, A. Schirmeisen, Multibond dynamics of nanoscale friction: the role of temperature, Phys. Rev. Lett. 104 (6) (2010) 066104.

[63] N.S. Tambe, B. Bhushan, Friction model for the velocity dependence of nanoscale friction, Nanotechnol. 16 (10) (2005) 2309–2324.
[64] M. Morita, T. Ohmi, E. Hasegawa, M. Kawakami, M. Ohwada, Growth of native oxide on a silicon surface, J. Appl. Phys. 68 (3) (1990) 1272–1281.
[65] M.R. Amirzada, A. Tatzel, V. Viereck, H. Hillmer, Surface roughness analysis of SiO_2 for PECVD, PVD and IBD on different substrates, Applied Nanosci. 6 (2016) 215–222.
[66] B.A. Verberne, C. He, C.J. Spiers, Frictional properties of Sedimentary rocks and natural fault gouge from the longmen shan fault zone, sichuan, ChinaFrictional properties of sedimentary rocks and natural fault gouge from the longmen shan fault zone, Bull. Seismol. Soc. Am. 100 (5B) (2010) 2767–2790.
[67] B. Verberne, C.J. Spiers, A.R. Niemeijer, J. De Bresser, D. De Winter, O. Plümper, Frictional properties and microstructure of calcite-rich fault gouges sheared at sub-seismic sliding velocities, Pure Appl. Geophys. 171 (10) (2014) 2617–2640.
[68] J. Chen, B.A. Verberne, C.J. Spiers, Interseismic re-strengthening and stabilization of carbonate faults by “non-dieterich” healing under hydrothermal conditions, Earth Planet. Sci. Lett. 423 (2015) 1–12.
[69] P. Baker, M. Kastner, J. Byerlee, D. Lockner, Pressure solution and hydrothermal recrystallization of carbonate sediments—an experimental study, Mar. Geol. 38 (1–3) (1980) 185–203.
[70] A. Niemeijer, C. Spiers, A microphysical model for strong velocity weakening in phyllosilicate-bearing fault gouges, J. Geophys. Res. Solid Earth 112 (B10) (2007).
[71] B. Carpenter, C. Collettini, C. Viti, A. Cavallo, The influence of normal stress and sliding velocity on the frictional behaviour of calcite at room temperature: insights from laboratory experiments and microstructural observations, Geophys. J. Int. 205 (1) (2016) 548–561.
[72] J.B. McClimon, Z. Li, D. Goldsby, I. Szlufarska, R.W. Carpick, The Effects of Humidity on the Velocity-Dependence and Frictional Ageing of Nanoscale Silica Contacts, (2023).
[73] J. Dziadkowiec, S. Javadi, J.E. Bratvold, O. Nilsen, A. Røyne, Surface forces apparatus measurements of interactions between rough and reactive calcite surfaces, Langmuir 34 (25) (2018) 7248–7263.
[74] J. Dziadkowiec, B. Zareeipolgardani, D.K. Dysthe, A. Røyne, Nucleation in confinement generates long-range repulsion between rough calcite surfaces, Sci. Rep. 9 (1) (2019) 8948.